North west cape-induced electron precipitation and theoretical simulation*

Zhen-xia Zhang(张振霞)[1,†], Xin-qiao Li(李新乔)[2], Chen-Yu Wang(王辰宇)[3], and Lun-Jin Chen[4]

[1] *National Earthquake Infrastructure Service, China Earthquake Administration, Beijing* 100045, *China*
[2] *Institute of High Energy Physics, Chinese Academic Sciences, Beijing* 100049, *China*
[3] *Peking University, Beijing* 100871, *China*
[4] *Department of Physics, University of Texas at Dallas, Richardson, Texas, USA*

(Received 16 April 2016; revised manuscript received 27 July 2016; published online 30 September 2016)

Enhancement of the electron fluxes in the inner radiation belt, which is induced by the powerful North West Cape (NWC) very-low-frequency (VLF) transmitter, have been observed and analyzed by several research groups. However, all of the previous publications have focused on NWC-induced > 100-keV electrons only, based on observations from the Detection of Electro-Magnetic Emissions Transmitted from Earthquake Regions (DEMETER) and the Geostationary Operational Environmental Satellite (GOES) satellites. Here, we present flux enhancements with 30–100-keV electrons related to NWC transmitter for the first time, which were observed by the GOES satellite at night. Similar to the 100–300-keV precipitated-electron behavior, the low energy 30–100-keV electron precipitation is primarily located east of the transmitter. However, the latter does not drift eastward to the same extent as the former, possibly because of the lower electron velocity. The 30–100-keV electrons are distributed in the $L = 1.8$–2.1 L-shell range, in contrast to the 100–300-keV electrons which are at $L = 1.67$–1.9. This is consistent with the perspective that the energy of the VLF-wave-induced electron flux enhancement decreases with higher L-shell values. We expand upon the rationality of the simultaneous enhancement of the 30–100- and 100–300-keV electron fluxes through comparison with the cyclotron resonance theory for the quasi-linear wave-particle interaction. In addition, we interpret the asymmetry characteristics of NWC electric power distribution in north and south hemisphere by ray tracing model. Finally, we present considerable discussion and show that good agreement exists between the observation of satellites and theory.

Keywords: North West Cape electron precipitation, wave–particle interaction, quasi-linear diffusion equation, ray tracing

PACS: 94.20.wj, 94.30.Tz, 93.85.Rt **DOI:** 10.1088/1674-1056/25/11/119401

1. Introduction

There are many factors that cause high-energy particle acceleration, precipitation, and short-term, sharp increases in particle count rates in radiation belts, including the influence of ground-based VLF electromagentic (EM) transmitters, lightning and thunderstorms, and ground nuclear testing. The primary mechanism of ground-based VLF EM transmission is that the emitted EM wave is transmitted across the atmosphere, expands into the ionosphere, and interacts with the energetic particles in the radiation belt. This interaction accelerates the particles by changing their momentum or scattering their pitch angle, which causes them to enter the bounce or drift loss cones LC_{drift}. As a result, a mass of energetic particles accumulates within a certain L-shell and yields particle-flux enhancement, which can be observed by the onboard particle detectors of satellites.[1–6]

Numerous experimental observations and theoretical interpretations of the electron-flux enhancement induced in the inner radiation belt by VLF ground-based transmitters have been reported.

For example, Kimura *et al.* have found strong correlations between the 0.3–6.9-keV electron fluxes observed by the EXOS-B satellite and the 0.3–9-kHz VLF wave emitted by the ground-based transmitter at SIPLE.[7] The observed instantaneous correlation between the VLF signal and the electron fluxes has been studied[8] and interpreted using wave–particle interaction theory,[9] which was applied to a test-particle model of a gyroresonant wave–particle interaction in order to calculate the precipitation characteristics of the particle flux induced by a VLF transmitter. Hence, it was found that the particle precipitation is controlled by the α distribution near the edge of the loss cone.

The Lualualei (NPM) VLF transmitter has been studied by Inan *et al.*,[10] who have suggested that the energetic electrons induced by this transmitter, which are scattered at the NPM longitude, continue to precipitate into the atmosphere as they drift toward the South Atlantic Anomaly. Further, Graf *et al.* have compared the precipitating fluxes with predictions based on ray-tracing analysis of the wave propagation

*Supported by the China Seismo-Electromagnetic Satellite Mission Ground-Based Verification Project of the Administration of Science, Technology, and Industry for National Defense and Asia-Pacific Space Cooperation Organization Project (APSCO-SP/PM-EARTHQUAKE).

†Corresponding author. E-mail: zxzhang@neis.cn

© 2016 Chinese Physical Society and IOP Publishing Ltd

and test-particle modeling of the wave-particle interaction.[11] Their results indicate that the precipitated flux of the >100-keV electrons induced by the NPM transmitter peak at $L \simeq 1.9$. They have also indicated that the detection rate is related to the orientation of the Detection of Electro–Magnetic Emissions Transmitted from Earthquake Regions (DEMETER)[12,13] particle detector, obtaining agreement between their observations and theory.

Several studies of the electron-precipitation belts induced by the North West Cape (NWC) VLF ground-based transmitter have also been conducted, and the events related to this transmitter are the focus of this paper. Based on readings from the DEMETER satellite, Sauvaud *et al.* have observed NWC-transmitter-induced enhancements in the 100–600-keV LC_{drift} electron fluxes at L values of 1.4–1.7.[14] These researchers have calculated the variation in the energy of the enhanced electron fluxes in response to changes in L using the first-order cyclotron resonance theory of wave–particle interaction; hence, they have obtained results consistent with observation. Further, Li *et al.* have analyzed the energy spectra of the NWC electron belts precisely using an on–off method, and explained the α range by considering the quasi-linear diffusion equation of wave-particle theory.[15] Independently of the DEMETER detection of the NWC-transmitter-induced electron enhancement of LC_{drift}, Gamble *et al.* have also examined the data for >100-keV quasi-trapped electron fluxes and reported similar enhanced electron counts from the 90° electron telescopes on the National Oceanic and Atmospheric Administration (NOAA) 15, 16, 17, and 18 Polar-orbiting Operational Environmental Satellite (POES), for the time period in which the NWC transmitter was broadcasting.[16]

In the early work by Kennel *et al.* on the pitch angle scattering of radiation-belt particles, the gyroresonant wave–particle interactions were thought to play a crucial role in the magnetosphere physics.[17] Further, scattering by chorus waves was studied as the dominant cause of diffuse auroral precipitation.[6] One of the theoretical models for numerically calculating the precession of waves inducing energetic particle precipitation is the quasi-linear diffusion equation. In particular, Summers *et al.* have developed a precise formula of quasi-linear diffusion coefficient corresponding to R- or L-mode EM waves which have a Gaussian spectral density and propagate in a hydrogen plasma.[18] These researchers have expanded the collisionless Vlasov equation for the particle-flux differential function to the second-order perturbation and obtained the diffusion equation form. In the inner radiation belt, the particle velocities are generally significantly larger than the typical phase velocities of the waves; therefore, pitch angle diffusion plays a dominant role in the wave–particle interaction.

In addition, many electron-belt effects induced by man-made VLF ground-based transmitters can be described using the theoretical model of wave–particle interaction. For example, Horne *et al.* have studied the mechanism behind the wave-induced electron acceleration in the outer radiation belt.[4] These researchers have shown that the electrons can be accelerated by EM waves at frequencies of a few kHz, which can also increase the electron flux by more than three orders of magnitude over an observation timescale of 1–2 d.

However, all of the previous analyses of the NWC-transmitter-induced particle precipitation have focused on particles with energies above 100 keV only. In this paper, we present a more comprehensive survey of energetic particles for a wider energy spectrum, including particles with energies below 100 keV. We will then simulate the wave–particle interaction process for NWC-induced electron precipitation using quasi-linear diffusion theory, which considers the α scattering and energy diffusion for different L values. We compare the simulation results to the observations from the DEMETER and NOAA satellites. Finally, we discuss the limitations of the theory.

2. Observations

The NWC ground station is located in the northwest corner of Australia with geographical coordinates of (21.82°S, 114.15°E), and geomagnetic coordinates of $(-31.96°, 186.4°)$, which emits electromagnetic waves with frequency of 19.8 kHz, a very narrow bandwidth and a large emission power of 1 MW.[15]

The DEMETER satellite was launched in June 2004 and is a low-altitude satellite with onboard detectors to measure local electric and magnetic fields and energetic particle populations.[12,13] This satellite, having a quasi-Sun-synchronous orbit, travels downward (from north to south) during local daytime and upward (from south to north) during local nighttime. The orbital period is 102.86 min.

Data on the NWC-induced electron belts have been obtained using DEMETER and analyzed.[15] These data indicate the presence of obvious wisp structures, which correspond to a spectrogram of NWC electrons distributed in five different L-value regions (see Fig. 10 in Ref. [9] for details). Thus, it has been confirmed that the electron precipitation belts are caused by EM waves emitted from the NWC transmitter. The L values for the NWC electron belts range from 1.5 to 2.2. The local pitch angle α for the NWC electron belts measured by the DEMETER detector is approximately 60°–110°, which corresponds to an equatorial pitch angle α_{eq} of 23.5°–25° at a latitude of 37° in the southern hemisphere.

The NOAA satellites are positioned in a polar orbit (inclination angle: 99°) at altitudes of 807–854 km. The con-

stituent particle detectors (Space Environment Monitor; SEM-2), which monitor the proton and electron fluxes at the satellite altitudes, consist of total energy detectors (TEDs) and medium energy proton and electron detector (MEPEDs). An MEPED is composed of eight solid-state detectors.

In addition to the wisp structure of the NWC-induced electron precipitation observed by the DEMETER satellite, we have investigated the observed data for the inner-radiation-belt electrons using data recorded in 2007 by NOAA satellites. Following the approach described in Ref. [16], we also present NWC-induced electron belts obtained from NOAA data in Fig. 1. This image shows the significant distributions of the 30–100- and 100–300-keV electron counts for the geographic position of the subsatellite point, for signals obtained in the operating period of 1 January to 31 May 2007. The background obtained during the non-operational period of 1 August to 31 December 2007 has been subtracted from these signal data. The ratios of the subtraction and background electron counts are also shown in the figure.

Note that waves from the NWC primarily propagate through the ionosphere at night.[19] Thus, we combined all the 16-s electron integral flux observations provided by the NOAA National Geophysical Data Center by summing the observation data obtained by the NOAA 15, 16, 17, and 18 POES at night (2200–0600 UT).

In contrast to Ref. [16], we exhibit the NWC electron belts in the lower-energy region (30–100 keV) in Figs. 1(a) and 1(c). These images indicate that the NWC transmitter induces not only electrons of >100 keV, but also those with energy <100 keV. Note that this is the first time that NWC-induced electron precipitation belts in the lower-energy range of 30–100 keV have been reported. In Fig. 2, we also present the effect of NWC transmission projected into the L-shell for electron observations in the two energy ranges of 30–100 keV and 100–300 keV, based on data from the NOAA satellites. The L-shell values are directly linked to the dynamic mechanism of the wave–particle interaction, and the L-shell distribution of the NWC electrons demonstrates that the 30–100-keV electrons are most likely induced by the NWC transmission in the 1.8–2.0 L-shell, whereas the 100-300-keV electrons are at 1.7–1.9. This result indicates that lower-energy electrons can be influenced by NWC EM waves in higher L-shells in the ionosphere. In addition, figure 2 also indicates that the the NWC electrons drift eastward above the Earth's surface, in accordance with the basic three-motion theory for charged particles in the ionosphere, where those motions are gyration, bounce, and drift. Furthermore, the 30–100- and 100–300-keV NWC electrons drift from 110°–160° and 110°–240° longitude, respectively. This behavior is likely to be caused by the different electron velocities. Note that, the higher the electron velocity is, the farther eastward in the ionosphere the electrons can travel.

Examples of NWC wisp structures observed by the DEMETER satellite are exhibited in Fig. 3, which displays various NWC electron precipitation belts obtained during NWC transmitter operation. Note that the background data when the NWC transmitter was deactivated are subtracted from these results.

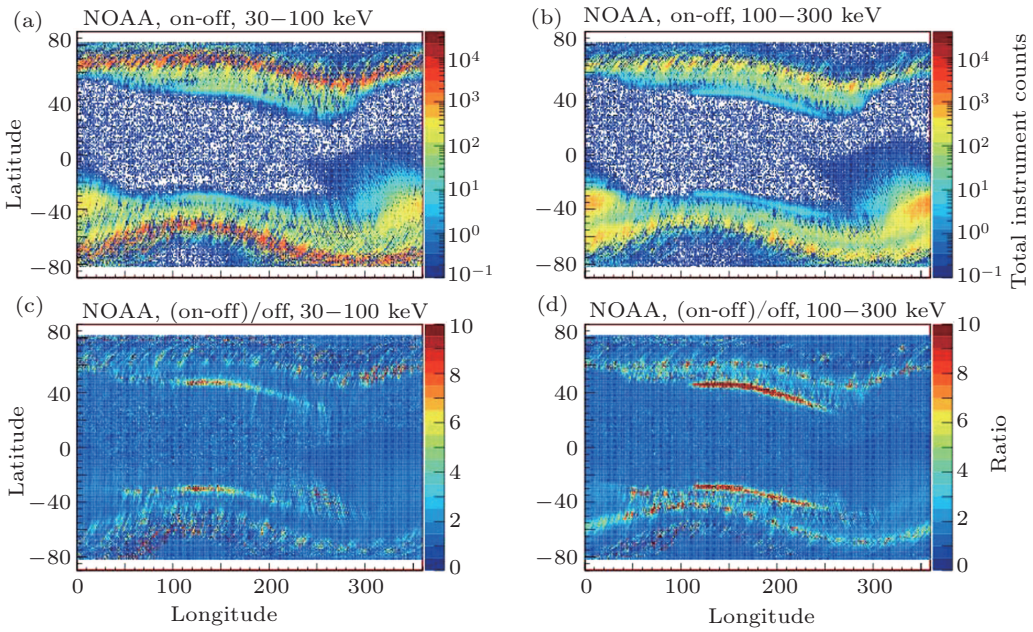


Fig. 1. Effects of NWC transmission for 30–100 and 100–300-keV electron observation data from NOAA satellites. (a) and (b) Electron counts for 1 January to 31 May 2007 with those for 1 August to 31 December 2007 subtracted. The data in each period are the sum of all 30–100- or 100–300-keV electron counts from the medium energy proton and electron detectors (MEPEDs) in the 90° telescopes for the given periods. (c) and (d) Ratio of subtracted data shown above to background electron counts for 1 August to 31 December 2007. The NWC was operating normally from 1 January to 31 May 2007.

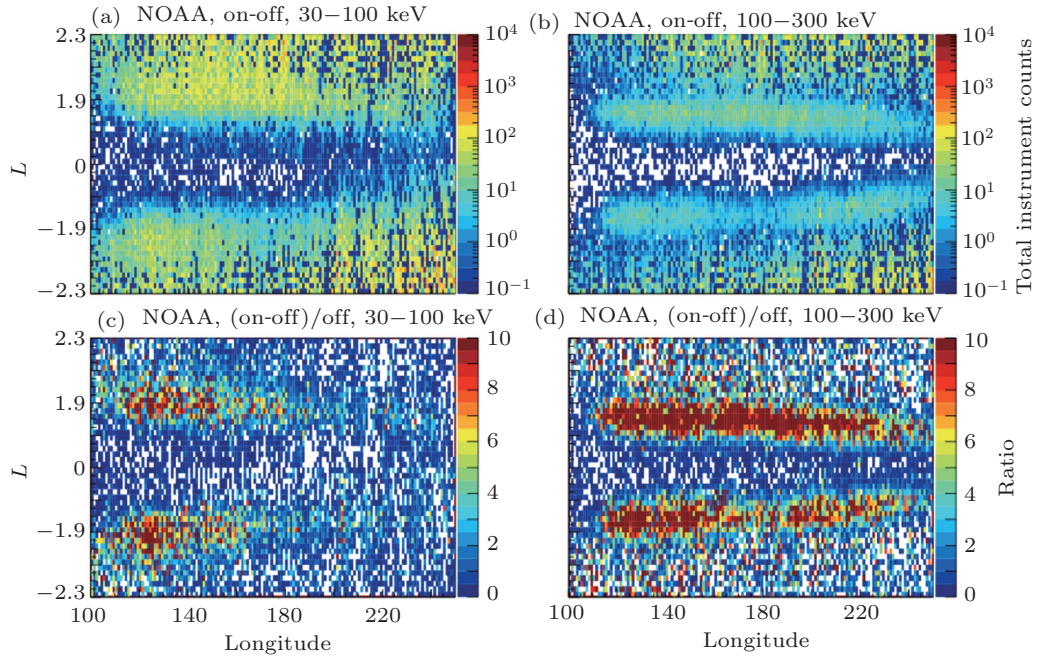


Fig. 2. Effect of NWC transmission projected in L-shell as indicated by 30–100- and 100–300-keV electron observations from NOAA satellites. (a) and (b) Electrons for 1 January to 31 May 2007, with those for 1 August to 31 December 2007 subtracted. The data in each period are the sum of all 30–100- or 100–300-keV electron counts from the 90° MEPEDs for the given periods. (c) and (d) Ratio of subtracted data shown above to background for 1 August to 31 December 2007. The NWC was operating normally from 1 January to 31 May 2007.

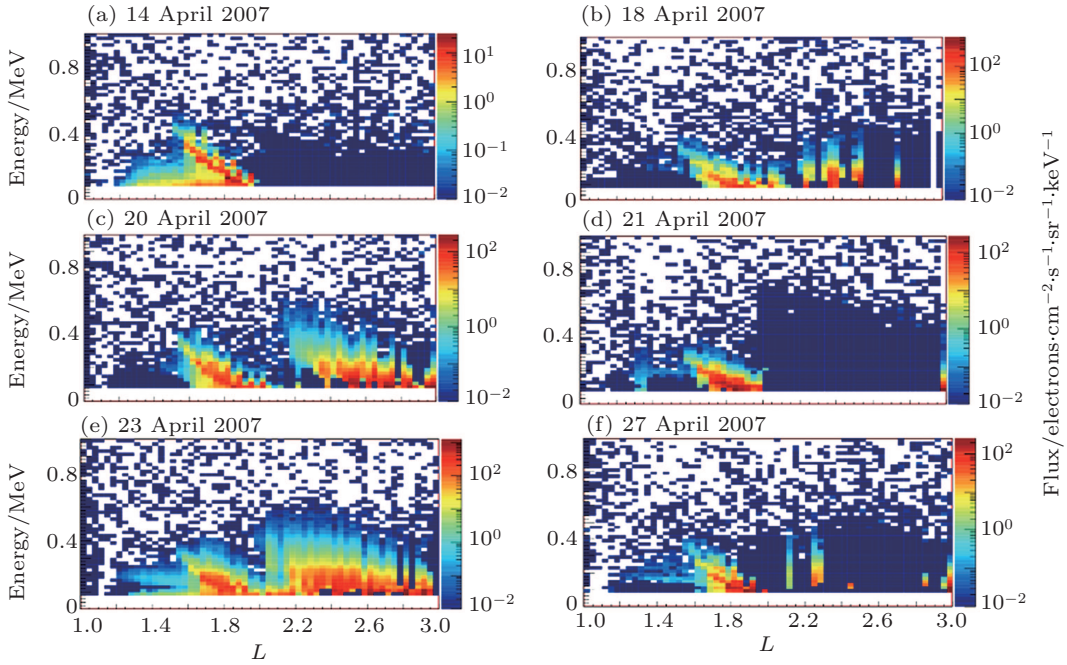


Fig. 3. Examples of NWC electron precipitation wisp structures after background effect is extracted from signal data obtained from IDP on board the DEMETER satellite. (a) 14 April 2007, (b) 18 April 2007, (c) 20 April 2007, (d) 21 April 2007, (e) 23 April 2007, and (f) 27 April 2007. Six examples of absolute flux measurements are given in units of electrons·cm^{-2}·s^{-1}·sr^{-1}·keV^{-1} during wisp events. The signal is adopted from data recorded in April 2007, when the NWC transmitter was operating, whereas the background data were obtained in July 2007, when the NWC transmitter was deactivated. For example, the first plot is the effect of the signal data in the NWC electron precipitation area on 14 April. Thus, the background data recorded in the same area on 14 July have been subtracted.

3. Verification of quasi-linear diffusion equation in wave–particle interaction theory

3.1. Quasi-linear models

Originating from the Fokker–Planck equation, the quasi-linear diffusion equation has been developed as a practical and convenient form.[20–23,45] Similar to the dipole field case, the diffusion equation used in this paper, which includes both pitch angle and momentum diffusion, is expressed as

$$\frac{\partial f}{\partial t} = \frac{1}{T(\alpha)}\frac{\partial}{\partial \alpha}\left[T(\alpha)\left(\langle D_{\alpha\alpha}\rangle\frac{\partial f}{\partial \alpha} + \langle D_{\alpha p}\rangle\frac{\partial f}{\partial p}\right)\right]$$

$$+\frac{1}{p^2}\frac{\partial}{\partial p}\left[p^2\left(\langle D_{p\alpha}\rangle\frac{\partial f}{\partial \alpha}+\langle D_{pp}\rangle\frac{\partial f}{\partial p}\right)\right]-\frac{f}{\tau}, \quad (1)$$

where

$$T(\alpha)=S(\alpha)\sin 2\alpha. \quad (2)$$

Here, $S(\alpha)$ is a function corresponding to the bounce frequency obtained from the bounce-averaged performance, which is estimated in a dipole field[25] such that

$$S(\alpha)=1.38-0.32(\sin\alpha+\sqrt{\sin\alpha}), \quad (3)$$

where τ is the electron lifetime, which is generally set to be a quarter of the bouncing time in the loss cone and f/τ is infinite outside the loss cone. The $\langle D_{\alpha\alpha}\rangle$, $\langle D_{pp}\rangle$, and $\langle D_{p\alpha}\rangle$ terms correspond to the bounce-averaged diffusion coefficients for the pitch angle diffusion, momentum diffusion, and their mixed term, respectively, having the following detailed formulae:

$$\langle D_{\alpha\alpha}\rangle=\frac{1}{S(\alpha_{\rm eq})}\int_0^{\lambda_{\rm m}}{\rm d}\lambda D_{\alpha\alpha}\frac{\cos\alpha}{\cos^2\alpha_{\rm eq}}\cos^7\lambda, \quad (4)$$

$$\langle D_{\alpha p}\rangle=\frac{1}{S(\alpha_{\rm eq})}\int_0^{\lambda_{\rm m}}{\rm d}\lambda D_{\alpha p}\frac{(1+3\sin^2\lambda)^{\frac{1}{4}}}{\cos\alpha_{\rm eq}}\cos^4\lambda, \quad (5)$$

$$\langle D_{pp}\rangle=\frac{1}{S(\alpha_{\rm eq})}\int_0^{\lambda_{\rm m}}{\rm d}\lambda D_{pp}\frac{(1+3\sin^2\lambda)^{\frac{1}{2}}}{\cos\alpha}\cos\lambda, \quad (6)$$

where $\lambda_{\rm m}$ denotes the latitude of the bounced-particle mirror point. Therefore, the phase space density is regarded as a function of equatorial pitch angle $\alpha_{\rm eq}$, the kinetic energy E, and the L-shell with the expression $f(\alpha_{\rm eq},E,L)$.

The wave-frequency spectrum density is assumed to obey a Gaussian distribution. Assuming the field-aligned electromagnetic wave, the closed analytical form of the local pitch-angle diffusion coefficient of the wave–particle interaction is derived as follows (see Ref. [18], Eqs. (33)–(35)):

$$\begin{aligned}D_{\alpha\alpha} &= \frac{\pi}{2}\frac{1}{\nu}\frac{\Omega_\sigma^2}{|\Omega_{\rm e}|}\frac{1}{(E+1)^2}\\ &\times\sum_s\sum_j\frac{R\left(1-\dfrac{x\cos\alpha}{y\beta}\right)^2|F(x,y)|}{\delta x|\beta\cos\alpha-F(x,y)|}\\ &\times{\rm e}^{-(\frac{x-x_{\rm m}}{\delta x})^2}, \quad (7)\\ \frac{D_{\alpha p}}{p} &= \frac{\pi}{2}\frac{1}{\nu}\frac{\Omega_\sigma^2}{|\Omega_{\rm e}|}\frac{\sin\alpha}{\beta(E+1)^2}\\ &\times\sum_s\sum_j\frac{R\left(\dfrac{x}{y}\right)\left(1-\dfrac{x\cos\alpha}{y\beta}\right)|F(x,y)|}{\delta x|\beta\cos\alpha-F(x,y)|}\\ &\times{\rm e}^{-(\frac{x-x_{\rm m}}{\delta x})^2}, \quad (8)\\ \frac{D_{pp}}{p^2} &= \frac{\pi}{2}\frac{1}{\nu}\frac{\Omega_\sigma^2}{|\Omega_{\rm e}|}\frac{\sin^2\alpha}{\beta^2(E+1)^2}\\ &\times\sum_s\sum_j\frac{R(x/y)^2|F(x,y)|}{\delta x|\beta\cos\alpha-F(x,y)|}\\ &\times{\rm e}^{-(\frac{x-x_{\rm m}}{\delta x})^2}, \quad (9)\end{aligned}$$

where E is the dimensionless particle kinetic energy given by $E=E_k/(m_\sigma c^2)=\gamma-1$, $\beta=v/c=[E(E+2)]^{1/2}/(E+1)$, $R=|\delta B_s|^2/B_0^2$ is the ratio of the energy density of the turbulent magnetic field to that of the background field, and B_0 is the Earth's magnetic field. Further, $x_{\rm m}=\omega_{\rm m}/|\Omega_{\rm e}|$, $\delta x=\delta\omega/|\Omega_{\rm e}|$, and $s=1$ for the R-mode wave, while $s=-1$ for the L-mode wave, $j=1,2,\ldots,N$ is the root number satisfying the resonance condition. We have

$$\omega_j-v\cos\alpha k_j=-s\frac{q}{|q|}\frac{|\Omega_\sigma|}{\gamma}, \quad (10)$$

$F(x,y)={\rm d}x/{\rm d}y$ ($x=\omega/|\Omega_{\rm e}|, y=ck_i/|\Omega_{\rm e}|$) is determined from the dispersion equation of the electrons or protons as follows:

$$\left(\frac{ck}{\omega}\right)^2=1-\frac{(1+\varepsilon)/\alpha^*}{(\omega/|\Omega_{\rm e}|-s)(\omega/|\Omega_{\rm e}|+s\varepsilon)}, \quad (11)$$

where

$$\alpha^*=\Omega_{\rm e}^2/\omega_{pe}^2, \quad (12)$$

is an important cold-plasma parameter; ε is the rest mass ratio of an electron and proton; $|\Omega_{\rm e}|=e|B|/(m_{\rm e}c)$ denotes the electron gyrofrequency, and $\omega_{pe}=(4\pi Ne^2/m_{\rm e})^{1/2}$ is the plasma frequency, where N denotes the particle number density in the ionosphere and is determined by formula $N=N_0\times(2/L)^4$ cm^{-3}, where N_0 is the value of $N@L=2$. according to Refs. [26] and [27].

3.2. Numerical method, initial and boundary conditions

We solve the bounce-averaged Fokker–Planck equation numerically on ($\alpha_{\rm eq}$, p) plane at different L. The domain of our simulation corresponds to $[0,\pi/2]$ in $\alpha_{\rm eq}$, [0 MeV, 1.5 MeV] in E_k, and $[1,3]$ in L. The grid points are chosen to be $200\times200\times100$ for equatorial pitch angle, momentum, and L-shell, respectively. These grid points are distributed uniformly in our simulation domain. Our time step in this simulation is 100 s.

Since mixed partial derivatives appear in our diffusion equation, we choose fully implicit finite difference method to keep our simulation stable (similar to Ref. [22]). Schematically, our equation takes the form

$$\frac{\partial f}{\partial t}=\boldsymbol{F}f, \quad (13)$$

where $\boldsymbol{F}$ represents the differential operator on the right-handside. The implicit finite difference method can be written as

$$\frac{f^{n+1}-f^n}{\Delta t}=\boldsymbol{F}f^{n+1}, \quad (14)$$

where n is the time index. By solving the linear equation

$$(\boldsymbol{I}-\Delta t\boldsymbol{F})f^{n+1}=f^n, \quad (15)$$

at each step, we can obtain numerical solution of f at arbitrary time. To reduce solving time at each step, we apply LU decomposition to the discretized equation before simulation starts.

In order to resolve the wave–particle interaction equations with mixed derivative term, many numerical simulation methods have been introduced.[28,45] Here our simulation time is only several hours, with the time step 100 s, so a conventional fully implicit finite difference method is enough in this work.

In the numerical simulation of the quasi-linear diffusion to the NWC electron belts, the initial diffusion function f_0 satisfies the empirical formula

$$f_0 = \sin\alpha_{\rm eq}\, {\rm e}^{-\frac{E-0.1}{0.2}}. \tag{16}$$

In our simulation, we apply Dirichlet boundary condition at $E_k = 0$ MeV, and Neumann boundary condition on other boundaries. For $\alpha_{\rm eq}$

$$\left.\frac{\partial f}{\partial \alpha_{\rm eq}}\right|_{\alpha_{\rm eq}=0} = 0, \qquad \left.\frac{\partial f}{\partial \alpha_{\rm eq}}\right|_{\alpha_{\rm eq}=\pi/2} = 0, \tag{17}$$

and for E_k

$$f|_{E_k=0\ {\rm MeV}} = f_0|_{E_k=0\ {\rm MeV}}, \qquad \left.\frac{\partial f}{\partial E_k}\right|_{E_k=1.5\ {\rm MeV}} = 0. \tag{18}$$

3.3. Simulation results

In order to simulate the NWC electron belts induced by whistlerwaves in the ionosphere, the following parameters are chosen for use in the quasi-linear wave–particle coupling model: a Gaussian wave spectrum center frequency $\omega/(2\pi) =$ 19.8 kHz; a wave amplitude $\delta b = 200$ pT, which is consistent with the calculated result obtained via the NWC EM wave propagation described by full-wave model analysis,[29,30] a semi-bandwidth of 500 Hz, which is approximately consistent with the observed values obtained from the electric-field instruments on board the DEMETER satellite, and an equatorial magnetic field $B = 3.11 \times 10^{-5}/L^3$ T, which is determined by a dipole model.

We still consider the effect of the bounce loss cone and drift loss cone in the numerical simulation on the NWC electron precipitation belts. The bounce loss cone $\rm LC_{bounce}$ depends on the L-shell according to the expression

$$\rm LC_{bounce} = \arcsin\sqrt{\frac{\left(\frac{6470}{6370L}\right)^3}{\sqrt{4-3\left(\frac{6470}{6370L}\right)}}}. \tag{19}$$

In theory, drift loss cone $\rm LC_{drift}$ varies with longitude; however, it is actually affected by many factors, such as the season or certain magnetic storms. In the local area above the NWC transmitter position, we will exhibit the effect of $\rm LC_{drift}$ value at approximately 5°, 10°, and 15°, respectively. The electron lifetime τ is generally set to be a quarter of the bouncing time in the loss cone and infinite outside the loss cone. But in inner radiation belt, the bounce loss cone is larger and the observed electrons by satellite come from precipitated electrons in loss cone. τ with too small a value will induce too weak an effect of electron precipitation in a certain time. So here we set τ value to be 60 s.

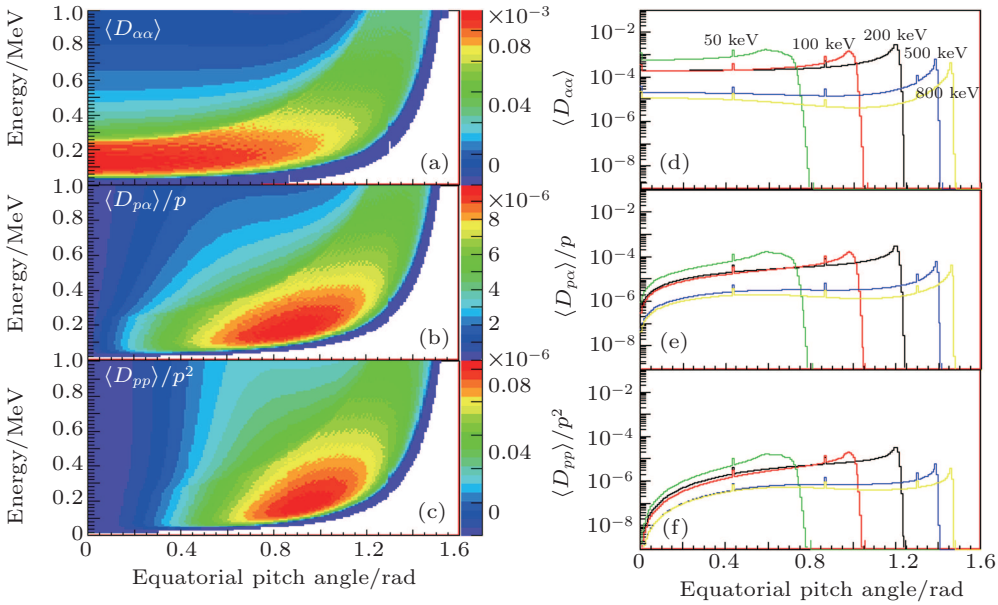


Fig. 4. Diffusion coefficient distributions with parameters: wave frequency $\omega/(2\pi) = 19.8$ kHz, wave amplitude $\delta b = 200$ pT, semiband width 500 Hz, and $N_0 = 3000$ counts/s. L-shell in panels (a)–(c): $L = 1.4$–2.0, L-shell in panels (d)–(f): $L = 2$. Five colorful lines denote the diffusion coefficient for electrons with 50 keV, 100 keV, 200 keV, 500 keV, and 800 keV, respectively.

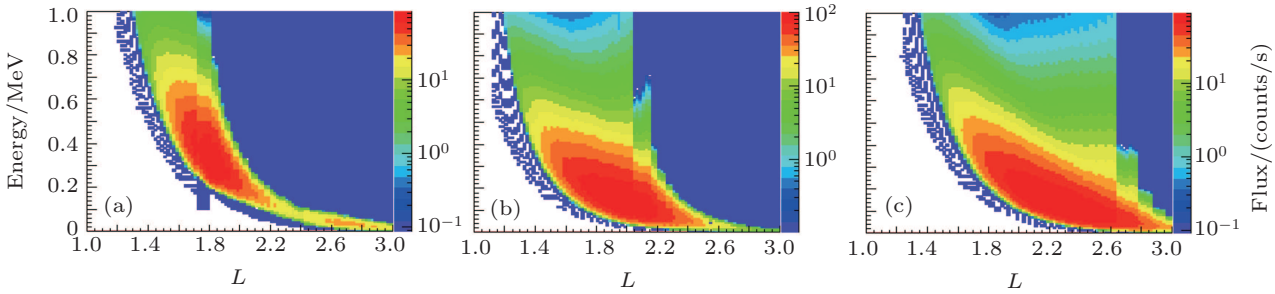


Fig. 5. Simulated NWC electron precipitation structures after subtraction of initial flux distribution from final flux distribution. Parameters used in simulation: frequency $\omega/(2\pi) = 19.8$ kHz; wave amplitude $\delta b = 200$ pT; semiband width 500 Hz; and $N_0 = 1000$ counts/s. The equatorial pitch angles α_{eq} used in the simulation ranging from 0.3 to 0.44, corresponding to the observation range by the DEMETER and NOAA satellites. The loss cones were set as follows: LC_{drift} = (a) 5°; (b) 10°; (c) 15°, all of which were with a bounce loss cone.

The bounce-averaged diffusion coefficients are exhibited in Fig. 4. We can see that the pitch angle diffusion is dominant and larger than momentum and mixed diffusion terms, and the pitch angle diffusion for electrons in $L = 1.4$–2.0 plays the strongest role in an energy range of 0.05–0.25 MeV.

By following the above numerical simulation method in Section 3.2, simulated results for 4-h evolution were obtained and are presented in Fig. 5. These results indicate the relatively good agreement with the satellite observation for the electron flux distribution, which is shown as a function of energy and L-shell (see Fig. 3). Identical parameters to those listed above were used in the simulation. Equation (1) was solved in the radial distance range from 1–3 Earth radii (R_E) and for equatorial pitch angle $\alpha_{eq} = 0$–$\pi/2$. The energy range does not vary with radial distance and was set to 0.05–1 MeV.

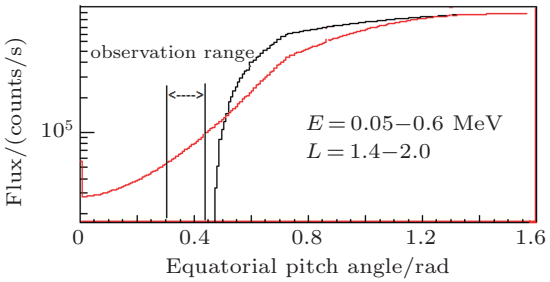


Fig. 6. Flux distribution of initial and final states during wave–particle interaction, corresponding to electrons with energy 0.05–0.6 MeV and L shell value 1.4–2.0. Other parameter values: wave frequency $\omega/(2\pi) =$ 19.8 kHz, wave amplitude $\delta b = 200$ pT, semiband width 500 Hz, and $N_0 = 3000$ counts/s. The DEMETER and NOAA satellite observation ranges from 0.3 rad to 0.44 rad.

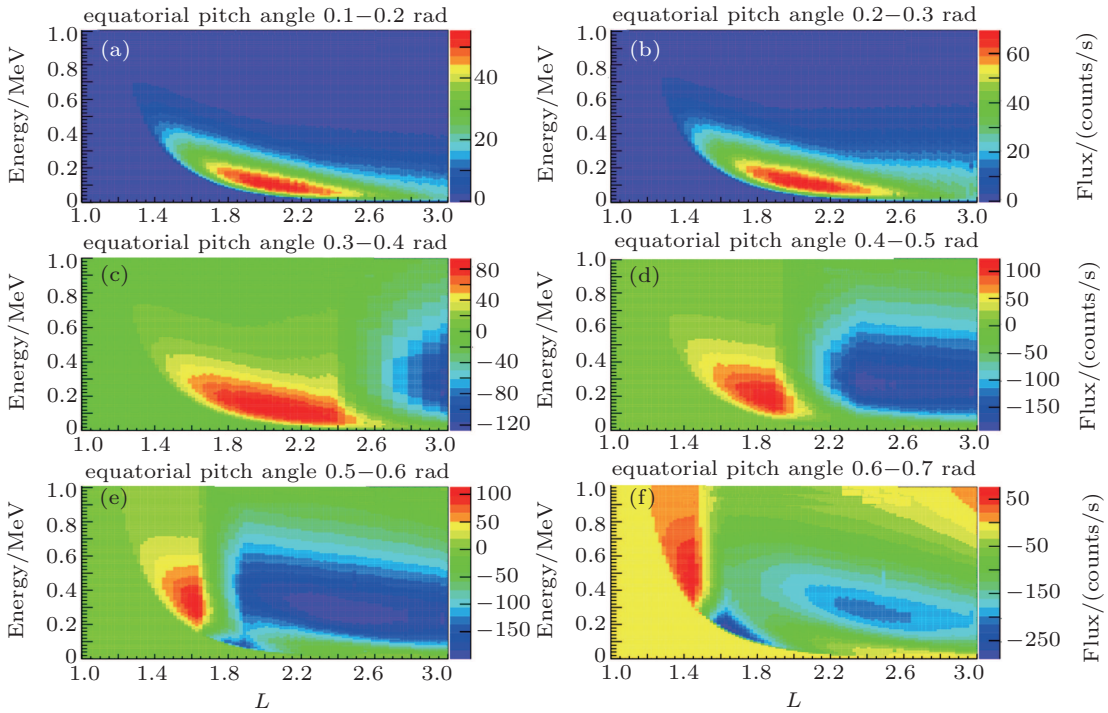


Fig. 7. Simulated electron precipitation structures after subtracting initial flux distribution from final flux distribution. Simulation parameters: Electromagnetic wave frequency $\omega/(2\pi) = 19.8$ kHz; wave amplitude $\delta b = 200$ pT; semi-band width 500 Hz; $N_0 = 1000$ counts/s; and equatorial pitch angles $\alpha_{eq} = 0.1$–0.2 rad (a), 0.2–0.3 rad (b), 0.3–0.4 rad (c), 0.4–0.5 rad (d), 0.5–0.6 rad (e), 0.6–0.7 rad (f).

As in the inner radiation belt, the radial diffusion scattering plays a small role in the total particle diffusion behavior. Note that all the plots in this figure correspond to $\alpha_{eq} = 17°$–$25°$ (that is 0.3 to 0.44 rad), which is consistent with detection range of the DEMETER satellite.[15] In the results shown in Fig. 5, the particle distribution depends on the $\sin\alpha_{eq}$; this is similar to the flat distribution inside the loss cone adopted in Ref. [31]. We still consider both the bounce and drift loss cone effects with LC_{drift} set to be: 5° (Fig. 5(a)), 10° (Fig. 5(b)), and 15° (Fig. 5(c)). The bounce loss cone is determined by Eq. (19). From Fig. 4, it can be seen that electron precipitation also takes place for the 50–100-keV range at higher L shell; this result is in agreement with the observations of the NOAA satellites.

Figure 6 is the flux distribution of initial (black) and final (red) states during wave particle interaction, corresponding to electrons with energy 0.05–0.6 MeV and L shell value 1.4–2.0. We can see that the satellite-observed electrons locate inside of loss cone when the electrons are scattered into loss cone mainly by a pitch angle diffusion mechanism.

Figure 7 is the simulated NWC electron precipitation for different equatorial pitch angle α_{eq} values of 0.1–0.2, 0.2–0.3, 0.3–0.4, 0.4–0.5, and 0.5–0.6 rad. It is apparent that the electron precipitation induced by the wave–particle interaction differs in different α_{eq} ranges. The simulation result obtained for an α_{eq} of 0.3–0.4 is located inside the IDP observation range on board the DEMETER satellite. Note that, at a higher α_{eq} range, it is easier for higher energy electrons to interact with VLF waves in the ionosphere. However, due to the pitch angle observation limitations of high-energy particle detectors and the lower density distribution of higher-energy electrons in space, it is possible that the electron precipitation induced by VLF waves is to some extent not observed by satellites.

4. Asymmetric distribution of the NWC electric field

The NWC electric field power distribution for the entirety of January 2007, as detected by the DEMETER satellite, is shown in Fig. 8. This figure shows that, at the altitude of the DEMETER satellite orbit, the L-shell of the NWC electric-field power covers 1.3–1.5 and 1.5–1.8 in the southern and northern hemispheres, respectively. This phenomenon of asymmetrical distribution of the NWC electric field in space is obvious.

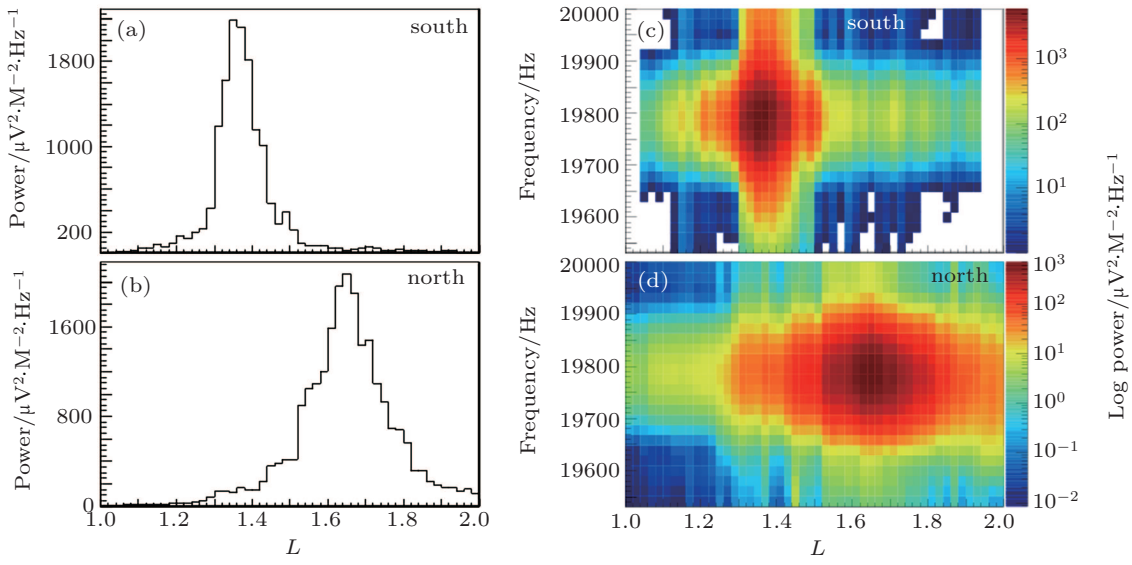


Fig. 8. NWC electric-field power distributions measured by DEMETER satellite in January 2007. (a) and (c) The distributions in south hemisphere, (b) and (d) the distributions in north hemisphere. Panels (a) and (b) are the two-dimensional distributions of NWC electric-field power projected by three-dimensional distributions in panels (c) and (d), respectively.

In order to explain this phenomenon, we use ray tracing model in a cold plasma in dipole magnetic field,[46–49] to simulate the NWC wave propagation path in magnetosphere. Electromagnetic waves with 19.8 kHz are launched at $L = 1.35$ close to NWC site on southern hemisphere, over a cone of 5 degrees with respect to the vertical direction of Earth's surface. The launch position is at geographic coordinate (21.82°S, 114.15°E) and geomagnetic coordinate (−31.96°, 186.4°). Figure 9 shows the simulated ray propagation paths. We can see that the L-shell values of NWC waves on north hemisphere at the conjugate latitude are higher. This asymmetry nature of NWC wave in southern and northern hemispheres is caused by the refraction effect of wave propagation in the inhomogeneous magnetosphere.

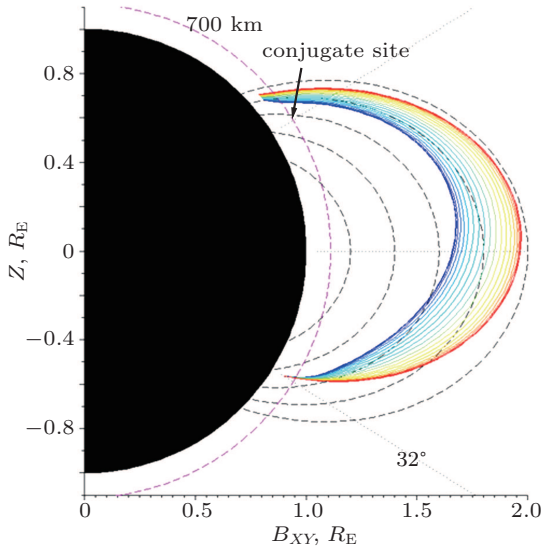


Fig. 9. Simulated NWC transmission path by ray tracing model. Electromagnetic wave with 19.8 kHz is launched over a transmission cone of 5° with respect to vertical direction.

5. Discussion and summary

In this work, in addition to the previously reported electron precipitation with 100–600-keV energy detected by the DEMETER satellite, we have still reported enhancement of the 30–100-keV electron flux observed by the NOAA satellites at night, when the powerful NWC VLF transmitter is broadcasting. We then performed a validity check using a theoretical model, i.e., the quasi-linear diffusion equation, and demonstrated approximate agreement with the satellite observation results.

Many factors influence the simulation results obtained using the quasi-linear diffusion equation, including the adopted wave semi-bandwidth, electron density. In Fig. 10, we show the simulated electron precipitation structure obtained for wave semi-bandwidths of 300 Hz, 500 Hz, and 1000 Hz and different electron densities. It is apparent that the simulated wisp structure is wider for a greater wave width. The simulated wisp structure moves toward to the lower L value with the electron density increasing. Thus, the parameter uncertainty, including loss cone, wave width and electron density, may consist of the factors which cause the difference of simulated result with the real wisp shapes observed via satellite.

Thus, these results indicate that the quasi-linear wave particle interaction model can describe an NWC electron precipitation wisp structure approximately, and can also explain the coupling characteristics of wave–particle interaction in a general sense. In particular, below the 0.1-MeV electron energy, the theoretical simulation results demonstrate agreement with the NOAA satellite observations shown in Fig. 2.

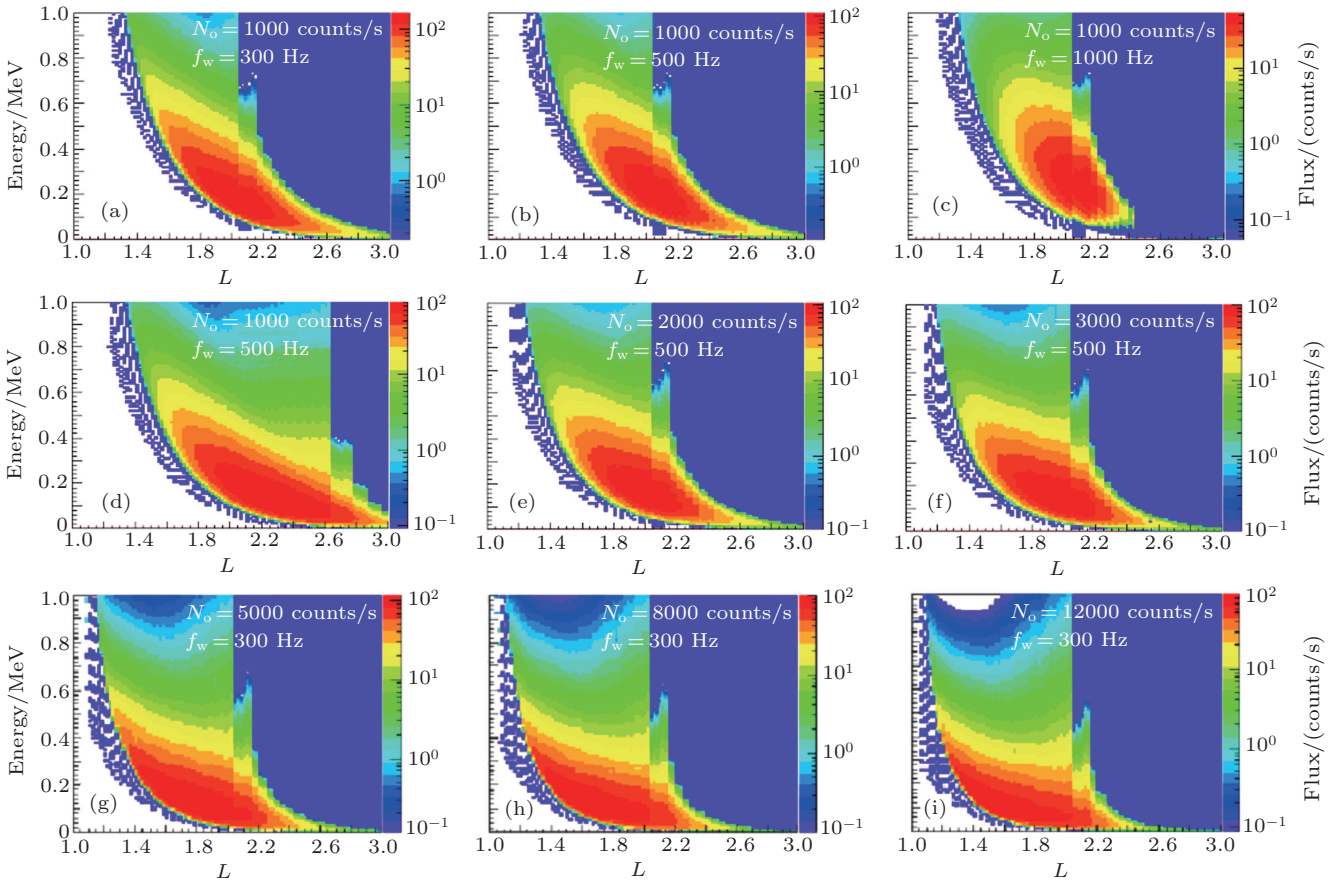


Fig. 10. Simulated electron precipitation structures after subtracting initial flux distribution from final flux distribution. Simulation parameters: electromagnetic wave frequency $\omega/(2\pi) = 19.8$ kHz; wave amplitude $\delta b = 200$ pT. The equatorial pitch angles α_{eq} range from 0.3 to 0.44, which is consistent with the DEMETER observation.

Electron precipitation or accumulation in the ionosphere may also be caused by both energy diffusion and radial diffusion in the L-shell.[32,33] However, in the inner radiation belt, the effect of radial diffusion on the L-shell can be omitted, especially at the satellite altitudes of hundreds of kilometers. The radial diffusion plays a large role in the wave–particle interaction only in the outer radiation belt.[5] In addition, when the theoretical simulation time is sufficiently long, e.g., having a duration of approximately 1 yr,[34] the radial diffusion in the L-shell evolution must be considered in the wave–particle interaction analysis in the inner radiation belt. Thus, significant attention is not paid to the effect of radial diffusion on the NWC electron belts in the analysis of the wave–particle interaction simulation conducted in this study.

However, we must note that the quasi-linear theory is thought to describe interactions between charged particles and small-amplitude broadband waves.[35] When the wave amplitude increases or the band becomes narrower, nonlinear effects such as phase trapping and bunching are more likely to become dominant, calling the use of quasi-linear theory into question.[36] Inan *et al.* have studied the nonlinear pitch angle scattering of energetic electrons by coherent VLF waves in the magnetosphere and compared their observations with linear theory.[37] They have also defined a quantity ρ, the ratio of the maximum absolute values of the wave and inhomogeneity terms, so as to differentiate between the linear and nonlinear interactions. Furthermore, Tao *et al.* have reported that the nonlinear interactions may be important near the equatorial plane, even for a moderate wave amplitude, and have shown that phase trapping is likely to occur when the wave-induced motion dominates the adiabatic motion.[38] These researchers subsequently used a test-particle code to confirm that the effect of the amplitude modulations should be considered in the quantitative treatment of nonlinear interactions between electrons and chorus waves.[39,40] There are other related works about dynamics of high-energy electrons interacting with whistler mode chorus emissions studied by test particle simulations.[41,42] Su *et al.* pointed out that the nonlinear physical processes, including boundary reflection effect, phase bunching and phase trapping, start to occur as the amplitude increases by studying the interaction between electrons and parallel-propagating monochromatic EMIC waves.[43] He then further presented that the nonlinear processes depend on the electron initial latitude and decrease or increase the loss rate predicted by the quasi-linear theory.[44] In addition, the azimuthal advection may play an important role in the radiation belt electron dynamics,[45] in the next work, we will study this effect and attempt to incorporate it into the theory model for research of ground-based induced electron precipitation belts.

Therefore, in our next work, we will attempt to adopt a non-linear theory model to further study this wave–particle interaction event, focusing on the quantitative calculation.

Also considering the real NWC electric-field power distributions in the L-shell for the south and north hemispheres observed by the DEMETER satellite, shown in Fig. 8, the wave–particle interaction is simulated numerically using the quasi-linear diffusion equations described above. The simulation results are shown in Fig. 11.

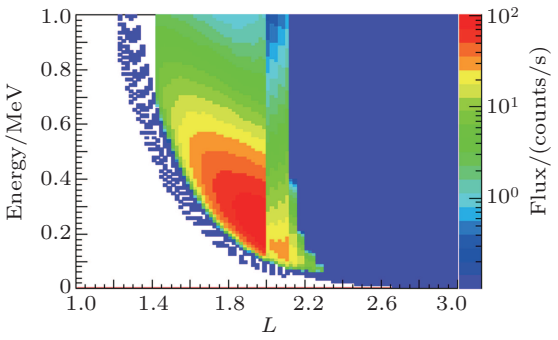


Fig. 11. Simulated NWC electron precipitation structure following subtraction of initial flux distribution from final flux distribution. The NWC electric-field power distributions in the L-shell in the south and north hemispheres are considered in the simulation process. Simulation parameters: electromagnetic wave frequency $\omega/(2\pi) = 19.8$ kHz; wave amplitude $\delta b = 200$ pT; semi-bandwidth 500 Hz; $N_0 = 1000$ counts/s. The equatorial pitch angles α used in the simulations range from 0.3 to 0.4, which is consistent with the value of the NWC electron precipitation wisp structures observed by the DEMETER and NOAA satellites. The bounce loss cone and $\mathrm{LC_{drift}} = 5°$ are set in the simulation.

From the simulation results shown in Fig. 10, the distribution trend of the NWC electron precipitation in the L-shell and the energy dimensions remain consistent with the observed wisp structure, although the simulated result is less accurate. This deviation from the observation results may be caused by a number of factors, including the influence of the wave bandwidth and cold plasma density. Additionally, the wave propagation effect in the ionosphere must be further studied in the next research stage. A comprehensive theoretical model that incorporates the wave propagation effect (such as the ray tracing model) and wave–particle interaction will facilitate a more complete and accurate approach to describing the electron precipitation in the radiation belt induced by the ground-based NWC transmitter.

In addition, we believe that analysis of the effects of the NWC VLF wave propagation and electron precipitation, along with the development of a comprehensive theoretical model, will facilitate the study of ground-based waves propagating into the ionosphere and interacting with high-energy particles in radiation belts. Based on wave–particle interaction theory, investigation of the EM disturbance in the ionosphere induced by seismic electromagnetic signals will be particularly useful, supposing that it is possible for seismic electromagnetic signals to propagate into ionosphere. As regarding to the influence of the EM waves emitted by seismic activities in wider

space, a large number of works have also been published on this topic, including studies based on satellite observation[50] and theoretical exploration research.[51–53]

Acknowledgment

This work is based on the observations of DEMETER and NOAA satellites, and we express our gratitude for the provision of the satellite data. The authors are grateful to Xin Tao, Qiugang Zong, and Yongfu Wang for useful discussion.

References

[1] Reeves G D, Baker D N, Belian R D, Blake J B, Cayton T E, Fennell J F, Friedel R H W, Meier M M, Selesnick R S and Spence H E 1998 *Geophys. Res. Lett.* **25** 3265
[2] Li X, Baker D N, Temerin M, Cayton T E, Reeves E G D, Christensen R A, Blake J B, Looper M D, Nakamura R and Kannekal S G 1997 *J. Geophy. Res.* **102** 14123
[3] Su Z, Xiao F, Zheng H, He Z, Zhu H, Zhang M, Shen C, Wang Y, Wang S, Kletzing C, Kurth W, Hospodarsky G, Spence H, Reeves G, Funsten H, Blake J and Baker D 2014 *Geophys. Res. Lett.* **41** 229
[4] Horne R B, Thorne R M, Shiprits Y Y, Meredith N P, Glauert S A, Smith A J, Kanekal S G, Baker D N, Engebretson M J, Posch J L, Spasojevic M, Inan U S, Pickett J S and Decreau M E 2005 *Nature* **437** 227
[5] Su Z P, Xiao F L, Zheng H N and Wang S 2011 *J. Geophys. Res.* **116** A04205
[6] Thorne R M, Ni B, Tao X and Horne R B 2010 *Nature* **467** 943
[7] Kimura, I, Matsumoto H, Mukai T, Hashimoto K, Bell T F, Inan U S, Helliwell R A and Katsufrakis J P 1983 *J. Geophy. Res.* **88** 282
[8] Imhof W L, Reagan J B, Voss H D, Gaines E E, Datlowe D W, Mobilia J, Helliwell R A, Inan U S, Katsufrakis J and Joiner R G 1983 *Geophys. Res. Lett.* **10** 361
[9] Inan U S, Chang H C and Helliwell R A 1985 *J. Geophys. Res.* **90** 359
[10] Inan U S, Golkowski M, Casey M K, Moore R C, Peter W, Kulkarni P, Kossey P, Kennedy E, Meth S and Smit P 2007 *Geophys. R. L.* **34** L02106
[11] Graf K L, Inan U S, Piddyachiy D, Kulkarni P, Parrot M and Sauvaud J A 2009 *J. Geophys. Res.* **114** A07205
[12] Parrot M, Benoist D, Berthelier J J, Blecki J, Chapuis Y, Colin F, Elie F, Fergeau P, Lagoutte D, Lefeuvre F, Legendre C, Lévêque M, Pincon J L, Poirier B, Seran H C and Zamora P 2006 *Planet. Space Sci.* **54** 441
[13] Sauvaud J A, Moreau T, Maggiolo R, Treilhou J P, Jacquey C, Cross A, Coutelier J, Rouzaud J, Penou E and Gangloff M 2006 *Planet. Space Sci.* **54** 502
[14] Sauvaud J A, Maggiolo R, Jacquey C, Parrot M, Berthelier J J, Gamble R J and Rodger C J 2008 *Geophys. Res. Lett.* **35** L09101
[15] Li X Q, Ma Y Q, Wang P, Wang H Y, Lu H, Zhang X M, Huang J P, Shi F, Yu X X, Xu Y B, Meng X C, Wang H, Zhao X Y and Parrot M 2012 *J. Geophys. Res.* **117** A04201
[16] Gamble R J, Rodger C J, Clilverd M A, Sauvaud J A, Thomson N R, Stewart S L, McCormick R J, Parrot M and Berthelier J J 2008 *J. Geophys. Res.* **113** A10211
[17] Kernel C F and Petschek H E 1966 *J. Geophys. Res.* **71** 1
[18] Summers D 2005 *J. Geophys. Res.* **110** A08213
[19] Starks M J, Quinn R A, Ginet G P, Albert J M, Sales G S, Reinisch B W and Song P 2008 *J. Geophys. Res.* **113** A09320
[20] Schulz M and Lanzerotti L 1974 *Particle Diffusion in the Radiation Belts*, in *Physics and Chemistry in Space* **7** (New York: Springer-Verlag) p. 533
[21] Tao X, Chan A A, Albert J M and Miller J A 2008 *J. Geophys. Res.* **113** A07212
[22] Subbotin D A and Shprits Y Y 2009 *Space Weather* **7** S10001
[23] Shprits Y Y, Chen L, Ukhorskiy A and Thorne R 2009 *J. Geophys. Res.* **114** A03219
[24] Su Z, Zheng H and Wang S 2010 *J. Geophys. Res.* **115** A06203
[25] Lenchek A, Singer S and Wentworth R 1961 *J. Geophys. Res. 12* **66** 4027
[26] Angerami J J and Thomas J O 1964 *J. Geophys. Res.* **69** 4537
[27] Inan U S, Chang H C and Helliwell R A 1984 *J. Geophy. Res.* **89** 2891
[28] in't Hout K J and Mishra C 2013 *Appl. Numer. Math.* **74** 83
[29] Lehtinen N G and Inan U S 2009 *Geophys. Res. Lett.* **36** L03104
[30] Zhao S F, Zhang X M, Zhao Z Y, Shen X H and Zhou C 2015 *Chin. J. Geophys.* **58** 2263 (in Chinese)
[31] Kennel C F 1969 *Rev. Geophys.* **7** 379
[32] Fälthammar C G 1965 *J. Geophys. Res.* **70** 2503
[33] Su Z, Zhu H, Xiao F, Zong Q, Zhou X, Zheng H, Wang Y, Wang S, Hao Y, Gao Z, He Z, Baker D, Spence H, Reeves G, Blake J and Wygant J 2015 *Nat. Commun.* **6** 10096
[34] Selesnick R S, Albert J M and Starks M J 2013 *J. Geophys. Res.* **118** 628
[35] Kennel C F and Engelmann F 1966 *Phys. Fluids* **9** 2377
[36] Bortnik J, Thorne R M and Inan U S 2008 *Geophys. Res. Lett.* **35** L21102
[37] Inan U S, Bell T F and Helliwell R A 1978 *J. Geophy. Res.* **83** 3235
[38] Tao X and Bortnik J 2010 *Nonlin. Processes Geophy.* **17** 599
[39] Tao X, Bortnik J, Thorne R M, Albert J M and Li W 2012 *Geophys. Res. Lett.* **39** L06102
[40] Tao X, Bortnik J, Albert J M, Thorne R M and Li W 2013 *J. Atmospheric Solar-Terrestrial Phys.* **99** 67
[41] Hikishima M, Yagitani S, Omura Y and Nagano I 2009 *J. Geophy. Res.* **114** A10205
[42] Omura Y and Summers D 2006 *J. Geophy. Res.* **111** A09222
[43] Su Z, Xiao F, Zheng H, Shen C, Wang Y and Wang S 2012 *J. Geophy. Res.* **117** A09222
[44] Su Z, Zhu H, Xiao F, Zheng H, Shen C, Wang Y and Wang S 2013 *J. Geophy. Res.* **118** 3188
[45] Su Z, Zheng H and Wang S 2010 *J. Geophy. Res.* **115** A06203
[46] Horne R B 1989 *J. Geophy. Res.* **94** 8895
[47] Chen L J, Bortnik J, Thorne R M, Horne R B and Jordanova V K 2009 *Geophys. Res. Lett.* **36** L22101
[48] Chen L J, Thorne R M, Li W and Bortnik J 2013 *J. Geophy. Res.* **118** 1074
[49] Xiao F L, Chen L J, Zheng H N and Wang S 2007 *J. Geophy. Res.* **112** A10214
[50] Zhang Z X, Li X Q, Wu S G, Ma Y Q, Shen X H, Chen H R, Wang P, You X Z and Yuan Y H 2012 *Chin. J. Geophys.* **55** 1581 (in Chinese)
[51] Zhang Z X, Wang C Y, Shen X H, Li X Q and Wu S G 2014 *Chin. Phys. B* **23** 109401
[52] Zhang Z X, Wang C Y Li Q, Wu S G 2014 *Acta Phys. Sin.* **63** 079401 (in Chinese)
[53] Wang P, Wang H Y, Ma Y Q, Li X Q, Lu H, Meng X C, Zhang J L, Wang H, Shi F, Xu Y B, Yu X X, Zhao X Y and Wu F 2011 *Acta Phys. Sin.* **60** 039401 (in Chinese)